Journal of Alloys and Compounds 1010 (2025) 177467

Contents lists available at ScienceDirect

Journal of Alloys and Compounds

journal homepage: www.elsevier.com/locate/jalcom

Explore the physical properties of the synthesized UiO-66, Zn-BiOBr, and Zn-BiOBr/UiO-66 heterostructures for optical applications

A. Farid [a,b], Hassan Nageh [c], T.S. Soliman [d,e], A. Khalid [f], Nour Marwan M. [g], Mohamed Taha [a,*]

[a] Nano Gate Company, 9254 Hodashaarawy, Al Abageyah, El Mukkatam, Cairo 11571, Egypt
[b] Central Metallurgical Research and Development Institute (CMRDI), Cairo, Egypt
[c] Nanotechnology Research Centre (NTRC), The British University in Egypt (BUE), Suez Desert Road, El-Sherouk City, Cairo 11837, Egypt
[d] Physics Department, Faculty of Science, Benha University, Benha 13518, Egypt
[e] Institute of Natural Sciences and Mathematics, Ural Federal University, Ekaterinburg 620000, Russian Federation
[f] Department of Basic Engineering Sciences, Faculty of Engineering at Shoubra, Benha University, Cairo, Egypt
[g] Faculty of Biotechnology, October University for Modern Sciences and Arts (MSA), Giza 12566, Egypt

ARTICLE INFO

Keywords:
UiO-66
Zn-BiOBr
Optical bandgap
Linear and non-lineal optical properties

ABSTRACT

The Zn-BiOBr/UiO-66 Heterostructures were prepared using a simple wet chemical method. Three heterostructures were prepared by varying the weight percentage of UiO-66 to Zn-BiOBr. The prepared materials' chemical compositions and phase structure were investigated using Fourier transform infrared (FTIR), X-ray diffraction (XRD), and X-ray photoelectron spectroscopy (XPS). Furthermore, the morphology was investigated via Field-emission scanning electron microscope (FE-SEM), energy dispersive X-ray (EDX), and elemental mapping techniques. The optical features were analyzed through UV–vis spectrophotometry. The bandgap energy was calculated using the Tauc equation and was found 4.24 eV for UiO66 and 2.17 eV for the ZnBiOBr composite. After combining the ZnBiOBr composite with the UiO66 material the bandgap energy of the composite decreased to 4.07, 3.94, and 3.75 eV after doping 10 %, 20 %, and 30 % UiO-66, respectively. Additionally, the refractive index of the Zn-BiOBr/UiO-66 heterostructure increases from 2.1520 for the UiO-66 composite to about 2.1929, 2.2254, and 2.2748 for 10, 20, and 30 % UiO66. Moreover, an enhancement was observed for other optical parameters like electronegativity, metallization, and optical conductivity. Besides, the W-DD model was used to investigate the nonlinear optical parameters, which showed an improvement in the first- and third-order nonlinear optical susceptibility, and nonlinear refractive index values with increasing UiO-66 content in the composite matrix.

1. Introduction

Metal-organic frameworks (MOFs) are hybrid materials consisting of metal ions or clusters bonded to organic ligands. MOFs possess characteristics of large surface areas and pore size that are adjustable, enabling various uses such as drug delivery, gas storage, separation, and water treatment [1]. Luminescent MOFs for molecular sensing are a major area of study for MOFs, particularly when employing guest-induced luminescent MOF materials [2]. Furthermore, MOFs exhibit interesting photocatalytic properties that can be harnessed for water purification and contaminant breakdown[3,4]. Upon light exposure, MOFs can generate reactive oxygen species that oxidize pollutants [5]. Among the different of MOFs, UiO-66, a zirconium-based MOF has attracted researchers' attention due to their exceptional characteristics, which include unprecedented structural stability independently to the ligand [6–8], high thermal stability, large surface area [9], photocatalytic activity [5], tunable pore aperture [10], and so on. UiO-66 also exhibits good chemical resistance, mechanical strength, and regeneration ability, making it robust and reusable [11]. These properties enable UiO-66 to effectively adsorb and degrade a range of pollutants in water [12–14] in addition to using in Opto-electronics applications and photovoltaic solar cells [14–16].

Bismuth oxyhalide typically forms layered three-dimensional structures that resemble flakes or spheres. The structure [X–Bi–O–Bi–X] forms tetragonal crystal-line lattices that are similar to matlockite [17]. Strong covalent bonds (Bi-O) and Van der Waals interactions between the halogen atoms produce a unique synergistic effect that leads to the unique optical, electrical, and structural features of these materials.

* Corresponding author.
E-mail address: Prof_mtm@yahoo.com (M. Taha).

https://doi.org/10.1016/j.jallcom.2024.177467
Received 8 August 2024; Received in revised form 17 October 2024; Accepted 7 November 2024
Available online 8 November 2024

Because the materials have significant polarizabilities, strong electric fields are generated within the crystalline network. When the halide doping the bismuth oxide structure changes, the band gap energy (Eg) of BiOX decreases with the halogen's ionization potential [18]. ultrathin BiOBr flakes based high-performance phototransistors show excellent Deep UV detection performances demonstrating its highly potential applications in UV optoelectronic devices [19]. Recently, Cai et.al [20] studied the optical absorption and photoactivity of ZnO nanoparticles with the incorporation of BiOBr composite material into the matrix and showed an enhancement to the absorption capacity of visible light for ZnO/BiOBr composites compared with pure ZnO nanoparticles, which indicates the ZnO/BiOBr composites could absorb more visible light than the ZnO sample. Also, Li et.al [21] synthesized BiOBr and BiOBr/ZnO composites using a simple hydrothermal approach, and modified their surfaces by plasma, which exhibited that the photocatalytic activity of pure BiOBr was increased by mixing BiOBr with ZnO, and further improvement was achieved through the plasma treatment. Meng et.al [22] have investigated the influence of the different weight percentages of BiOBr composite on the optical, photoactivity, and structure features of ZnO nanoparticles and found a reduction of the optical band gap value of the ZnO from 3.2 eV to about 2.95 eV with the addition of 50 % BiOBr, and the BiOBr/ZnO composites exhibited high photocatalytic performances toward Rhodamine B degradation under visible-light irradiation. Ali and Motawea [23] fabricated a BiOBr/ZnO/WO_3 heterojunction via the hydrolysis solvothermal process method, and found that the BiOBr/ZnO/WO_3 heterojunction is a highly effective visible-light photocatalyst for phenol degradation, outperforming single-phased WO_3, ZnO, or BiOBr as well as binary mixture photocatalysts, with a remarkable 90 % phenol degradation efficiency.

Overall, UiO-66 possesses a promising combination of properties as a visible-light-responsive and robust and extensive investigations have been carried out to study its chemical features, although these materials' optical properties are still inadequate. Here, we synthesize UiO-66 conjugated with Zn-BiOBr at various ratios and study its physico-chemical characteristics. Additionally, investigate the prepared materials' linear and non-linear optical characteristics.

2. Experimental section

2.1. Materials

Bismuth nitrate pentahydrate ($Bi(NO_3)_3.5H_2O$, 98 %), Cetyltrimethylammonium bromide (CTAB, 98 %), ethylene glycol (EG, 99.5 %), zinc acetate dihydrate ($Zn(CH_3COO)_2{\cdot}2\,H_2O$, 98 %), zirconium oxychloride octahydrate ($ZrOCl_2 \cdot 8\,H_2O$, 98 %), and sodium hydroxide pellets (NaOH, 97 %) were supplied by Loba Chemie Pvt Ltd, India. Terphthalic acid ($C_6H_4(COOH)_2$) and benzoic acid (C_6H_5COOH, 99 %) were obtained from Chem-Lab Analytical, Belgium. Hydrochloric Acid Fuming 37 % For Analysis EMSURE® ACS,ISO,Reag. Ph Eur, Absolute ethanol ACS, ISO, Reag, and N,N Dimethylformamide For Analysis Emsure® Acs,Iso,Reag. Ph Eur (DMF) were obtained from Merck, Germany. All the chemicals were used without further treatment for all the experiments.

2.2. Material preparations

2.2.1. Synthesis of Zn-doped BiOBr

A one-pot solvothermal process was used to prepare Zn-doped BiOBr [24]. Briefly, CTAB (0.05 M, EG solution) act as a template and Br-source then, Bi(NO3)3.5H2O was added in a 1:1 mol ratio with CTAB. Subsequently, zinc acetate was added to the mixture with a Zn/Bi molar ratio of 1:10. The resulting solution was magnetically stirred for 60 minutes at ambient temperature. Subsequently, the mixture was transferred to a Teflon-lined stainless steel autoclave and subjected to a solvothermal treatment (160 °C for 12 hours. After naturally cooling to room condition, the products were separated by centrifugation at 10, 000 rpm for 20 min (Hermle Z32HK, Germany) then Then repeatedly washed with deionized water and absolute ethanol. Finally, the sample was dried at 60 °C overnight which was labeled as ZB.

2.2.2. Synthesis of UiO-66 nanocrystalline

Solvothermal method was used for preparation of UiO-66 [25]. Briefly, dissolution of 0.05 M terephthalic acid, 0.04 M $ZrOCl_2.8H_2O$, and 0.05 M benzoic acid in DMF with the addition of HCl. After that, the mixture was stirred for half an hour at room temperature. Subsequently, the solution was transferred to Teflon lined autoclave reactor, sealed, and heated in an oven at 120°C for 48 hours. The resulting white pellets were collected via centrifuge (Hermle HKZ32, Germany) thoroughly washed with DMF, and further washed with ethanol to eliminated the unreacted materials. Finally, activating the UiO-66 in a vacuum oven at 80 °C for 12 hours, resulting in a white solid product.

2.2.3. Synthesis of Zn-BiOBr/UiO-66 nanocomposites

The Zn-BiOBr/UiO-66 nanocomposites were prepared using a simple wet chemical method. Three composites with different UiO-66 contents were synthesized by adjusting the weight percentage of UiO-66 to ZB [26]. For the composite with a ZB: UiO-66 wt ratio of (70:30), known as ZBU-30 %, the synthesis procedure was as follows: UiO-66 nanocrystalline was dispersed in deionized water through ultrasonication. Subsequently, ZB was added to the suspension and agitated for an additional 10 minutes. The resulting suspension was then transferred to Teflon-lined autoclave and heated at 90 °C for 6 hours. The precipitate obtained was filtered and dried in a vacuum oven at 80°C overnight. When the UiO-66 content was set at 10 %, 20 % and 30 %, the resulting composite of Zn-BiOBr/UiO-66 was labeled as ZBU-10 %, ZBU-20 %, and ZBU-30 % respectively for simplicity. Fig. 1.

2.3. Physico-chemical characterization

The prepared samples' Fourier transform mid-infrared (ATR/FTIR) spectra were obtained on Vertex 70-RAM II (Bruker Analytical, Germany). FTIR/ATR spectra were collected at room temperature, covering a 400–4000 cm^{-1} range. The phase and crystalline structure of the prepared materials was characterized via Empyrean Malverpanalytical, Netherland X- ray diffraction, with 2-Theta (5.0^o - 85^o), with step size 2-Theta: 0.04 and at (Kα) = 1.54060 Å., Morphology was performed Field Emission Scanning electron microscope (FE-SEM, Quattro S, Thermo Scientific), Furthermore, the elemental composition of the prepared materials were investigated using Energy Dispersive X-ray (EDX) and elemental Mapping. Utilizing X-ray photoelectron spectroscopy (XPS, ESCALAB 250Xi, Thermo Fisher, USA), the chemical state and electronic structure of the photocatalysts were verified. The UV–vis optical absorption spectra of prepared materials were measured via UV-Vis spectrophotometer UV-Vis spectrophotometer (Cary series UV-Vis- NIR, Australia), in a range of 200–800 nm. Photoluminescence (PL) Investigations were conducted at room temperature with laser wave length 320 nm via Lumina Fluorescence Spectrometer- Thermo-Scientific.

3. Results and discussion

3.1. Physico-chemical characterization

FTIR investigation was used to explore the coexistence of UiO-66 with Zn-doped BiOBr in nanocomposites. According to Fig. 2, the FTIR spectrum for pure Zn-BiOBr reveals key peaks, such as the broad band located between 3745 cm^{-1}–3610 cm^{-1} assigned to O-H stretching vibration coordinated with Bi^{3+}, indicating the presence of moisture [27, 28]. The peaks within range of 1000–1500 cm^{-1} are attributed to the Bi-Br bond in BiOBr [29]. The significant absorption band at 501 cm^{-1} is attributed to the Bi–O stretching mode [30]. Zinc doping introduces an additional peak at 427 cm^{-1}, which indicates Zn–O bond stretching

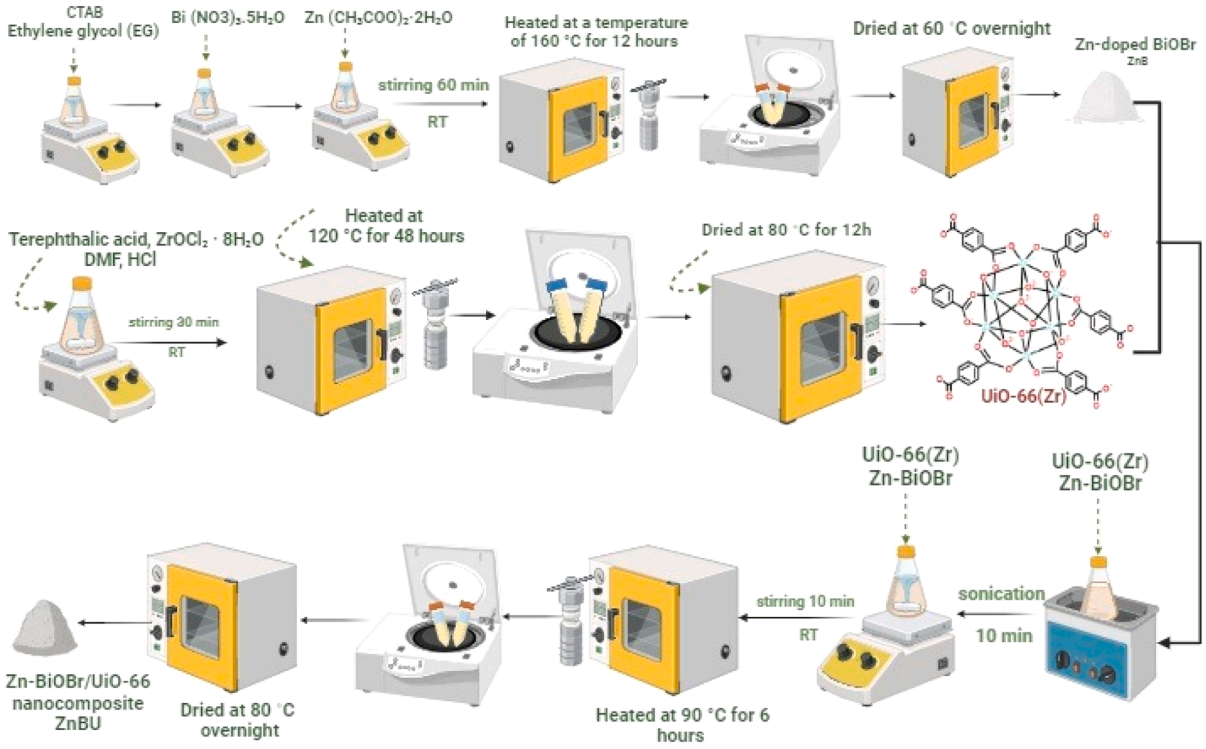

Fig. 1. A schematic depicting the fabrication process.

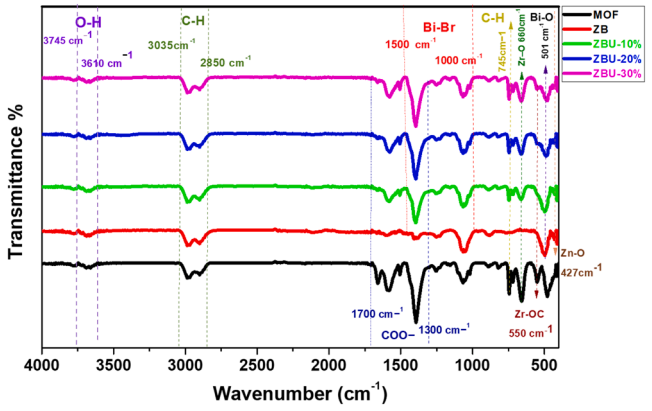

Fig. 2. FTIR spectra of Zn-BiOBr, UiO-66, and Zn-BiOBr/UiO-66 photocatalysts.

vibration. The FTIR spectrum for UiO-66 is characterized by several distinct peaks, the prominent peaks related to O–C–O symmetric and asymmetric stretching vibration of COO− group can be detected at 1393 cm^{-1} and 1586 cm^{-1} while, the small peak observed at 1505 cm^{-1} ascribes the vibration of C═C in benzene ring and the peak appear at 1660 cm^{-1} is related to C═O [27,31–33]. peak at 745 cm^{-1} is attributed to the vibration modes of C-H furthermore, the band at about 550 cm^{-1} was ascribed to Zr-(OC) asymmetric stretching. Moreover, the bands at 660 and 475 cm^{-1} represent Zr–O and Zr–OH, respectively [31,33,34]. In composites of Zn-BiOBr with varying proportions of UiO-66 ranging from 10 % to 30 %, the critical observation is that the intensity of the COO group stretching vibrations in the range of 1300 cm^{-1} to 1700 cm^{-1} emerged and its intensity increased with increasing in UiO-66 percent. This indicate that the ratio of UiO-66 influences its interaction with Zn-BiOBr, implying that higher concentrations of UiO-66 lead to stronger bonding or a more robust integration of the two components as the UiO-66 percentage rises [27]. Additionally, the peaks associated with Zr-O, Zr-OC and Zr-OH in the metal-organic framework become evident and more pronounced and increase in intensity as the MOF percentage increases in ZBUs.

XRD patterns were used to investigate the crystal structure and chemical composition of prepared of Zn-BiOBr, UiO-66, as ZBU-10 %, ZBU-20 %, and ZBU-30 % nanocomposites Fig. 3**a**. Briefly, the XRD pattern of UiO-66 shows that three distinctive peaks at $2\theta = 7.31°$, 8.39°, and 25.61° confirming that the pure phase of UiO-66 was successfully synthesized [6,25,35]. The peaks of Zn-BiOBr at 10.91°, 21.63°, 25.21°, 31.73°, 32.31°, 39.31°, 46.37°, and 57.21° could be attributed to the (001), (002), (101), (102), (110), (112), (200), and (212) facets of the tetragonal phase of BiOBr (JCPDS: 01–085–0862). For ZBU Nanocomposites the XRD patterns were displayed the characteristic peaks of Zn/BiOBr with peak at 7.31° which, assigned to UiO-66. The peak intensity was increase upon increasing amount of UiO-66, indicating formation and compounding of ZB and UiO-66 to form heterostructure between each other.

The XPS Spectra was utilized to investigate the elemental constituents and chemical state of pure UiO-66, Zn/BiOBr, and ZBU 20 % Fig. 3**b**. The pure UiO-66 displayed the characteristic peaks of O, Zr, and C and the pure Zn/BiOBr showed The main characteristic peaks of Bi, Br, Zn, O, and C. while the ZBU 20 % spectrum confirms the coexistence of Br, O, Bi, Zn, C, Zr ZBU 20 % (Fig. 3**b**).

The O1s high resolution XPS of BiOBr is consisting of three main peaks centering at: 533.23 eV, 530.96 eV and 530.23 eV. The peak at 533.23 eV is corresponding to oxygen species attached on the surface such as OH groups, which is result of alkane synthesis condition. Furthermore, the peak at 530.96 eV is corresponding to the Bi-O bond in the BiOBr, and the peak at 530.23 eV is reasonably assigned to the oxygen vacancies [36]. While, O1s in pure Uio-66 is composed of three peaks centering at: 530 eV, 531.38 eV, and 533.023 eV. The peak at 530 eV is corresponding to Zr-O group. The peak at 531.38 eV is corresponding to chemisorbed oxygen, and the peak at 533.023 eV is reasonably assigned to the O-C═O group [37]. Upon conjugation between ZB and UiO-66 the peak at 530.96 eV for Zn-BiOBr was shifted to

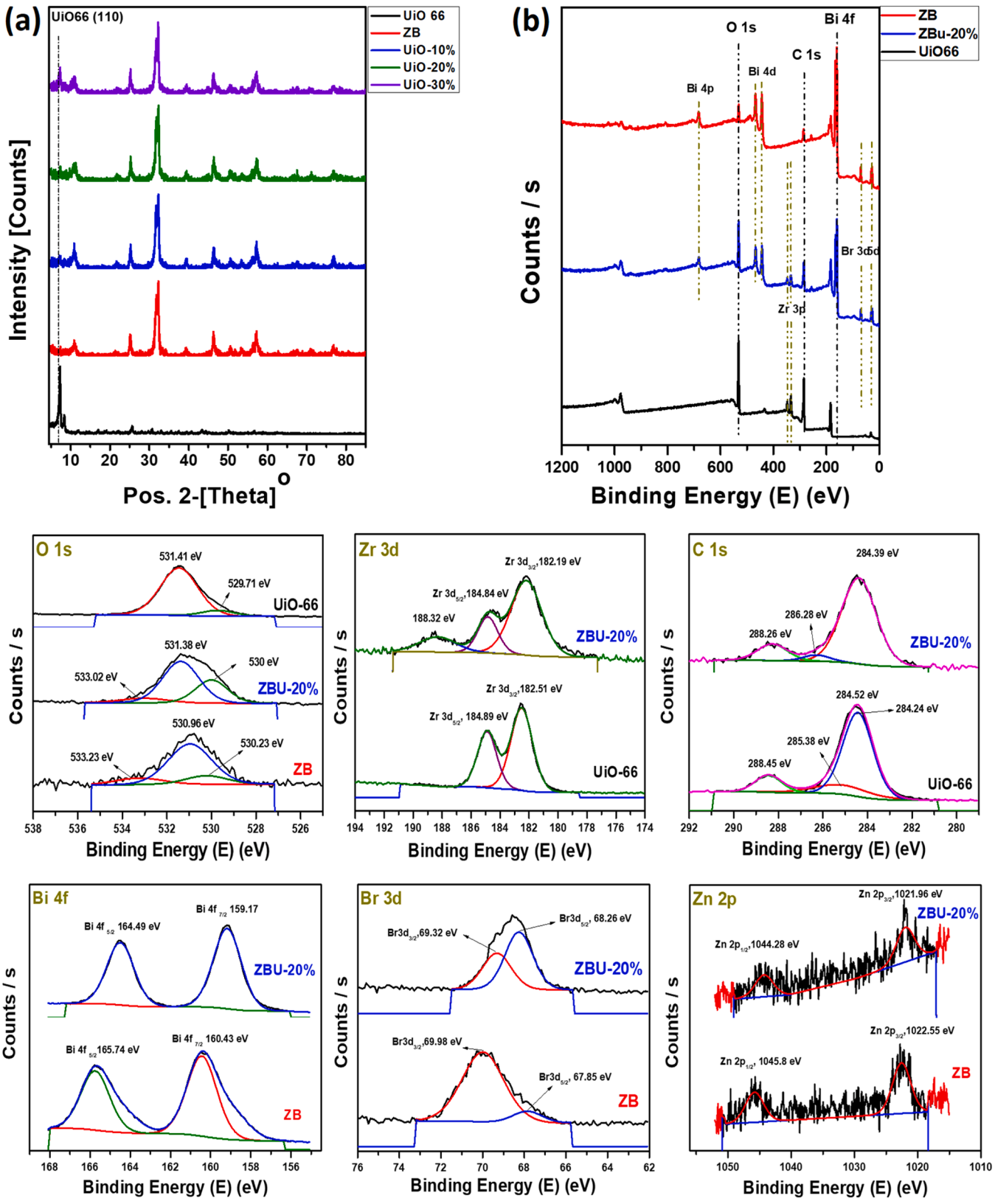

Fig. 3. (a) The XRD patterns of Zn-BiOBr, UiO-66, ZBU-10 %, ZBU-20 %, and ZBU-30 %, (b) the fully scanned XPS spectra of Zn-BiOBr, UiO-66, and ZBU-20 %, and the high resolution XPS spectra (O 1 s, Zr 3d, C 1 s, Bi 4 f, Br 3d, and Zn 2 P) of Zn-BiOBr, UiO-66, and ZBU-20 % respectively.

531.41 eV and peak at 530.23 was shifted to 529.71 eV due to the interaction and conjugation between ZB and UiO-66. Additionally, the Zr 3d spectrum of UiO-66 can be fitted by two contributions for Zr $3d_{3/2}$ and Zr $3d_{5/2}$ located at approximately 182.51 eV and 184.89 [38] a slight shift was observed after conjugation with ZB. the C 1 s spectrum displays three peaks, located at around 288.45, 285.38 and 284.24 eV, which can C═O, C-C, and C═C, respectively [39].

the XPS spectra of Bi 4 f for ZB can be fitted at 160.43 and 165.74 eV, which were attributed to Bi 4 $f_{7/2}$ and Bi 4 $f_{5/2}$, respectively. Two peaks corresponding to Br $3d_{5/2}$ and Br $3d_{3/2}$ were derived at 67.85 and 69.98 eV, respectively, from the Br 3d spectra as shown in Fig. 3 [36,40,41]. Two peaks of Zn 2 $P_{3/2}$ and Zn 2 $P_{1/2}$ were derived at 1022.55 eV and 1045.8 eV, respectively, from the Zn 2 P spectra as shown Fig. 3 [42]

The SEM technique was used to illustrate the morphology of the as prepared materials (Fig. 4**).** Briefly, the pure Zn/BiOBr (Fig. 4**a**) exhibited as a homogenous micro-like flower shape (average diameter approximately 4:6 μm) with thin nano leaves (70±10 nm), The elements Bi, O, Br, and Zn were observed in the corresponding EDX investigation, confirming the synthesis of Zn doped BiOBr in a pure phase. Additionally, pure UiO-66 (Fig. 4**b**) showed homogenous spheroidal nanoparticles with particle size ranged 35:50 nm and the elements Zr, O, and C were observed in the corresponding EDX investigation. While, the ZBU nanocomposite materials (Fig. 4**(c, d, and e)**) depicts overlapping of micro flower structure of Zn/BiOBr with 0D UiO-66 resulting in immediate interaction between the Zn-BiOBr and UiO-66 components at the interface, which is desirable for charge transfer and the formation of UiO-66/Zn-BiOBr heterostructures. Furthermore, the EDX results showed co-existence of Zn-BiOBr elements (Bi, O, Br, and Zn) and UiO-66 constituents (Zr, O, and C) which aligns with the findings of the XPS. Moreover, Fig. 4**f** showed the elemental mapping of ZBU-20 %. The homogeneous distribution of ZB and UiO-66 among each other produced a homogenous heterostructure, as demonstrated (Fig. 4**f**).

3.2. Optical properties

3.2.1. Optical absorption and band gap

The absorption Spectra of Zn-BiOBr, UiO-66, ZBU-10 %, ZBU-20 %, and ZBU-30 % are illustrated in Fig. 5**a.**

Zn-BiOBr has an absorption spectrum characterized by a strong absorption at a maximum wavelength of about 354 nm, while the UiO-66 material is characterized by an absorption edge in the UV region with a maximum at about 266 nm, which is consistent with the literature. [43,44]. When Zn-BiOBr is conjugated with UiO-66, the absorption edge of the UiO-66 material shifts to a lower wavelength value with the appearance of a broad peak at about 350 nm, which is related to the Zn-BiOBr composite. This shift increases as the UiO-66 material concentration increases in the Zn-BiOBr. The extension of the absorption edge with the x-axis for the pure MOF is about 324 nm which is shifted to 350, 372, and 387 nm for the Zn-BiOBr conjugated with 10, 20, and 30 % UiO-66, respectively. As Fig. 5**b** illustrates, all tested materials were evaluated using an excitation wavelength of $\lambda = 320$ and their PL emission showed in the range 350–600 nm. Briefly, pure UiO-66 shows a highest PL emission at about 378 nm, indicating the high re-combination rate of photo-generated carriers. The Zn-BiOBr PL peak's lowest intensity suggested that the material had a higher level of photocatalytic activity. Upon conjugation between Zn-BiOBr and UiO-66, the PL intensity decreased, indicating a significant inhibition of electron–hole pair recombination in comparison of pure UiO-66. These results are according well with the previous studies [26,45].

The absorption data was used to plot the Tauc's relation between $(\alpha h\upsilon)^2$ and the incident photon energy hν as follows:

$$(\alpha h\upsilon)^2 = constant(h\upsilon - E_g) \quad (1)$$

where α is the absorption co-efficient and E_g is the direct bandgap energy [46]. As illustrated in Fig. 6**a**, the E_g value for UiO-66 material is about 4.24 eV, which is consistent with the literature [43,44]. While, the E_g value for the Zn-BiOBr composite is about 2.17 eV, which is near the values reported in the literature [21,22]. After combining the ZB with the UiO-66 the optical bandgap energy of the composite was about 4.07 eV, 3.94 eV, and 3.75 eV after conjugation at 10 %, 20 %, and 30 % UiO-66, respectively. These findings indicate that the incorporation of UiO-66 material into the Zn-BiOBr leaves first shifted the band gap towards the UV region and then redshifted to the visible region with increasing UiO-66 concentration. This concluded the improvements in the absorption of electromagnetic radiation in the ZBU composite as compared to UiO-66 material alone. Furthermore, to explain the mechanism of photocatalytic activity, it is necessary to confirm the valence band (VB) and conduction band (CB) potentials of UiO-66 and Zn-BiOBr and heterosturcture. As shown in Fig. 6b, c, and d, the valence band edges were obtained by VB-XPS spectra. It is observed that the VB potentials of the pure UiO-66 and Zn-BiOBr are at 2.08 and 0.98 eV, respectively while, the ZBU-20 % was 0.72 eV. Based on the results of DRS, the band edge positions of the conduction band (CB) of Zn-BiOBr, UiO-66, and ZBU-20 % heterostructure can be evaluated using the following equation[47].

$$ECB = \quad EVB - \quad Eg \quad (2)$$

According to the results of DRS, the band gap energies (E_g) of UiO-66, Zn-BiOBr, and ZBU-20 % were −2.18 eV, −1.19 eV, −3.22 eV, respectively.

The metallization criteria (M), linear refractive index (n), electronegativity (Δχ), and optical basicity (Λ) of the prepared materials are dependent on the bandgap energy through the following relations [48,49]:

$$M = \sqrt{\frac{E_g}{20}} = 1 - \frac{n^2 - 1}{n^2 + 2} \quad (3)$$

$$\Delta\chi = 0.2688\ E_g \quad (4)$$

$$n = -\ln(0.102\Delta\chi) \quad (5)$$

$$\Lambda = 1.59 - 0.2279\ \Delta\chi \quad (6)$$

M is a mathematical parameter that is used to show the prepared material's tendency toward metallization. An insulator is a material whose M value is greater and approaches unity, whereas a material becomes more metallic when its M value declines [49]. As seen in Table 1, the metallization criterion for the ZB is about 0.33, which indicates the near-metallic behavior of the ZB material, and for the UiO-66, it is about 0.46, which indicates the insulating of the MOF material, and this value is decreased with the combination of UiO-66 with the ZB composite to about 0.45, 0.44, and 0.43 after doping with 10, 20, and 30 % UiO-66, respectively.

Moreover, the optical electronegativity (Δχ) indicates that the bonding in the material is covalent or ionic, depending on whether its value is low or high, respectively [50]. From Table 1, the Δχ value of the ZB is about 0.58 and 1.14 for the UiO-66 which decreases with increasing the UiO-66 concentration. The combination between the ZB composite and UiO-66 causes an increase in the index of refraction of the UiO-66 and decreases in the index of refraction of the ZB composite; 2.8218 (ZB), 2.1520 (UiO-66), 2.1929 (ZBU-10 %), (2.2254 (ZBU-20 %), to about 2.2748 (ZBU-30 %). The n and Λ values increased as the UiO-66 combined with ZB composite with higher contents of the UiO-66 material, due to the decrease of the optical electronegativity of the material.

3.2.2. Refractive index and extinction coefficient

The refractive index (n) and the extinction coefficient (k) are related to the materials' reflectivity and attenuation or absorption coefficient, respectively, and are two of the most essential optical factors. Both

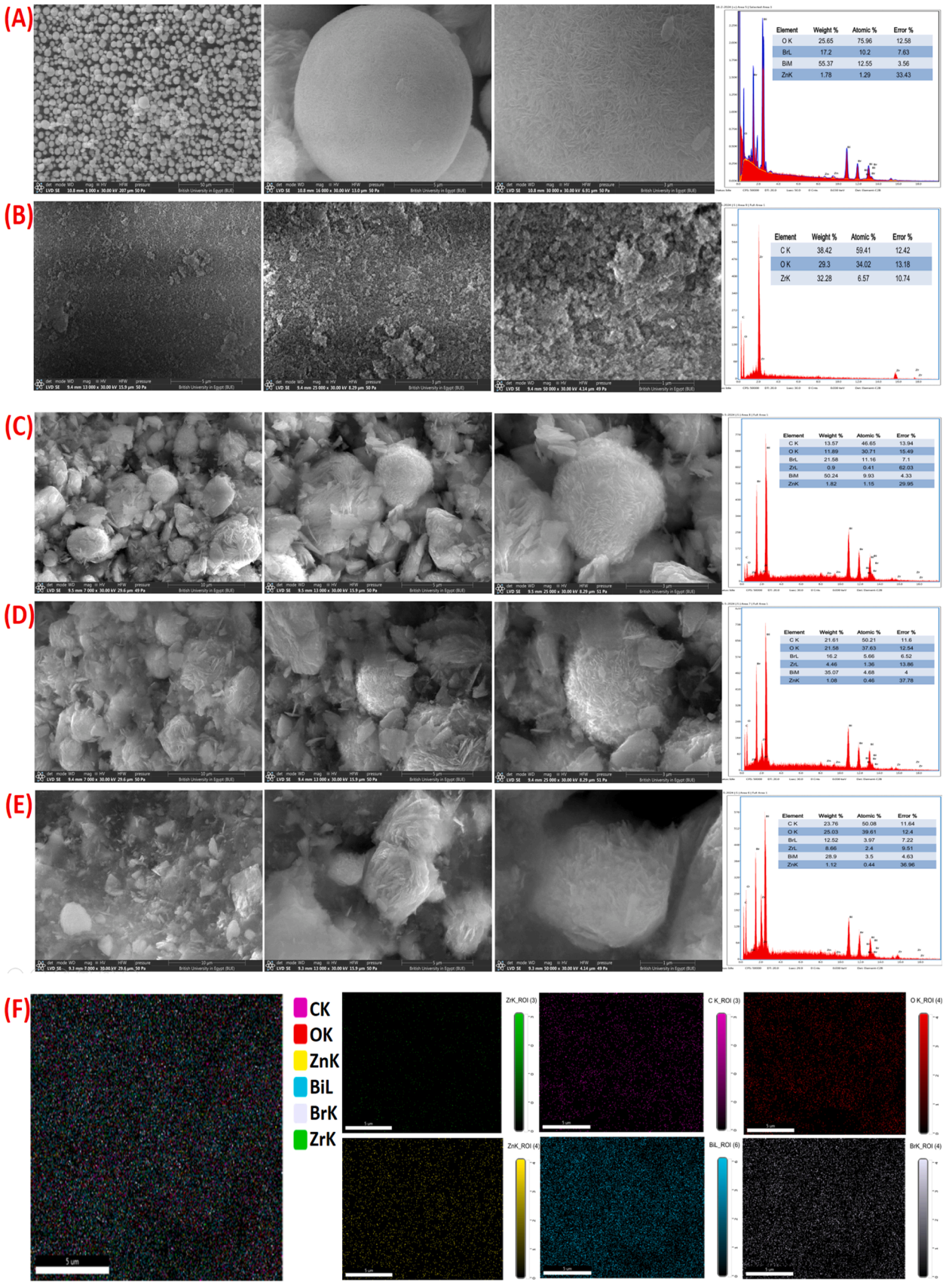

Fig. 4. (a) The SEM images at different magnifications with corresponding EDX spectrum of Zn-BiOBr, UiO-66, ZBU-10 %, ZBU-20 %, and ZBU-30 % (a, b, c, d, and, e) respectively, (F) the elemental mapping images of ZBU-20 %.

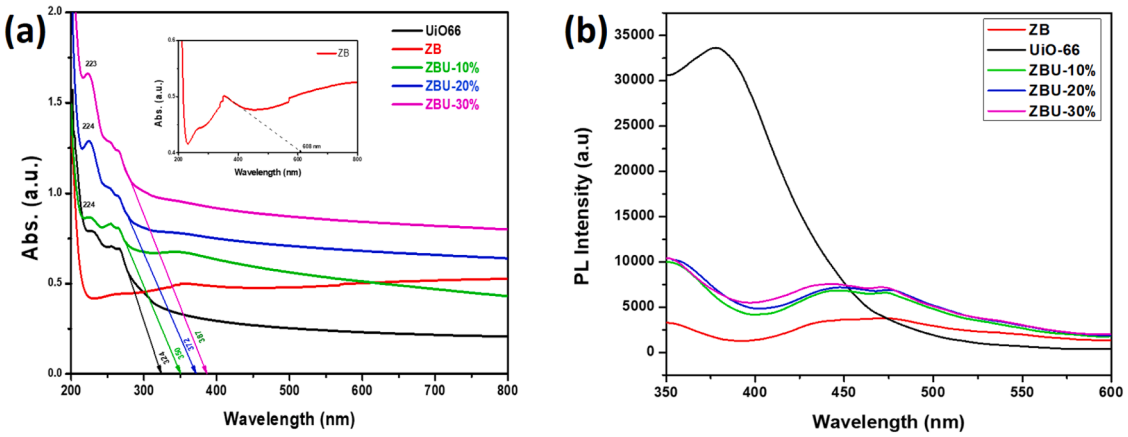

Fig. 5. The absorption spectra (a), and PL spectra (b) of Zn-BiOBr, UiO-66, ZBU-10 %, ZBU-20 %, and ZBU-30 %.

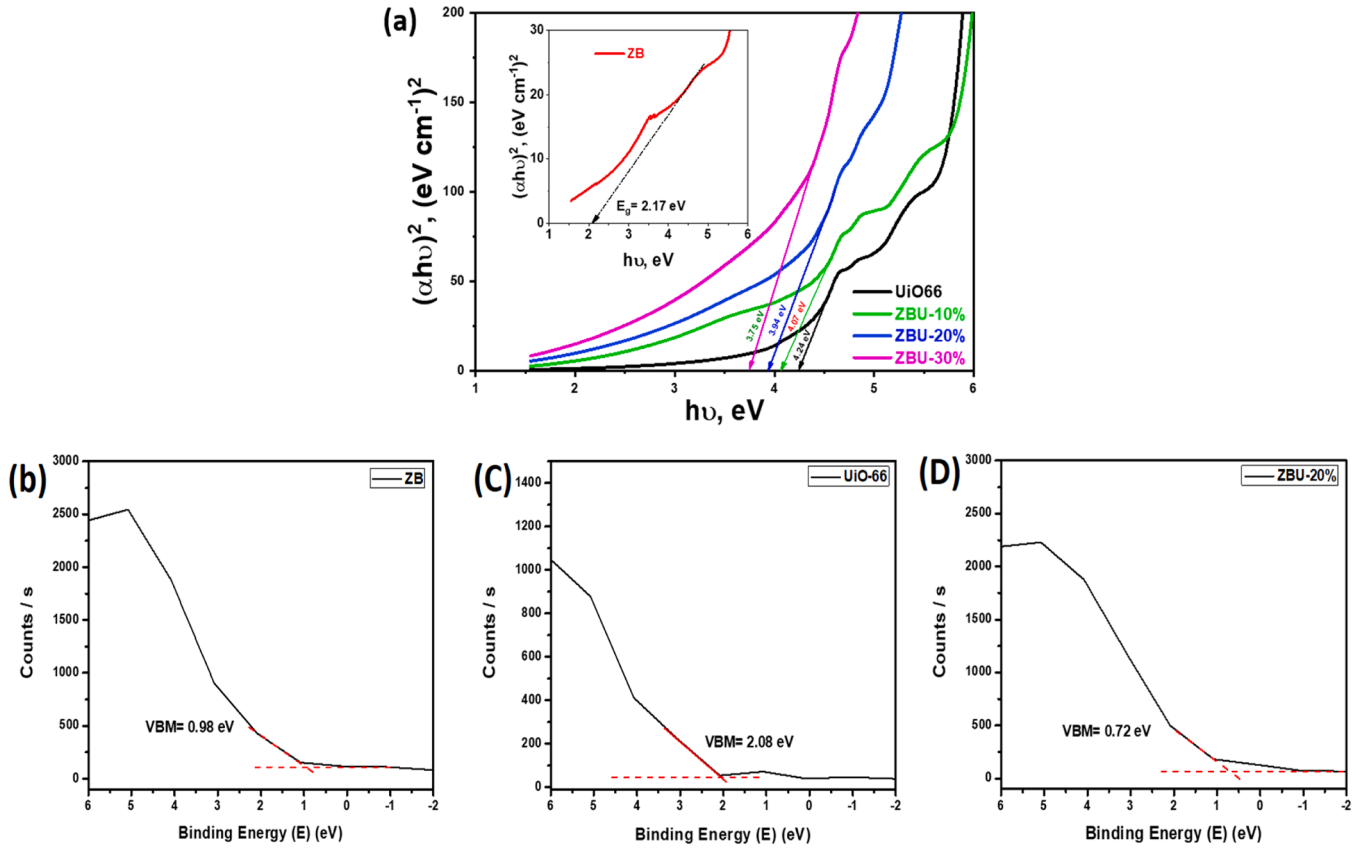

Fig. 6. (a) The plot of $(\alpha h\upsilon)^2$ vs. hυ of Zn-BiOBr, UiO-66, ZBU-10 %, ZBU-20 %, and ZBU-30 %. The valance band-XPS spectra of ZB, UiO-66, and ZBU-20 % a, b, and c respectively.

Table 1
optical parameters of Zn-BiOBr, UiO-66, ZBU-10 %, ZBU-20 %, and ZBU-30 %.

Sample ID	E_g (eV)	VBM (eV)	CBM (eV)	M (E_g)	M (n)	Δχ	Λ	n
UiO−66	4.24	2.06	−2.18	0.46	0.45	1.14	1.330	2.1520
ZBU−10 %	4.07	-	-	0.45	0.44	1.09	1.341	2.1929
ZBU−20 %	3.94	0.72	−3.22	0.44	0.43	1.06	1.349	2.2254
ZBU−30 %	3.75	-	-	0.43	0.42	1.01	1.360	2.2748
ZB	2.17	0.98	−1.19	0.33	0.30	0.58	1.457	2.8218

factors are related to each other through the following relations [51,52];

$$n = \frac{1+R}{1-R} + \sqrt{\frac{4R}{(1-R)^2} - k^2} \tag{7}$$

$$k = \frac{\alpha\lambda}{4\pi} \tag{8}$$

The reflectance ($R = 1 - \sqrt{T * e^A}$) was investigated through the absorption (A) and transmission (T) data obtained from the UV–visible spectra. As a function of the incident light wavelength, the n and k dependencies are represented in Fig. 7.

It was shown that *n* increases with increasing the amount of the UiO-66, as illustrated in the inset of Fig. 7**a**. Moreover, in the UV region (200 ≤ λ≤ 275 nm), n has a higher value due to the resonance effect, that results from the interaction of the incoming electromagnetic-radiation and the electrons polarization, as the incident photons frequency becomes equal to the plasma frequency [53,54]. The refractive index exhibits anomalous dispersion in this region. Moving towards the visible region (300 ≤ λ≤ 800 nm), the value of n decreases exponentially. However, at higher wavelengths, the decrease in *n* value is slight and appears to remain constant. The absorption of the electromagnetic waves became less, and most of the incident energy was reflected. As shown in Fig. 7**b,** based on this data, it appears that *k* decreases as the wavelength of incident photons increases, and seems constant for the pure UiO-66 NPs sample in the visible region. The k value then begins to rise with the insertion of UiO-66, rises with the UiO-66 additives to the Zn-BiOBr, and rises significantly at the highest value of (ZBU-30 %). The high value of the refractive index makes it useful as an anti-reflective coating in solar cell devices.

3.2.3. *Optical dielectric parameters and optical conductivity*

The complex dielectric constant is a basic feature of the material, and it has two components: real (ε′) and imaginary (ε″), as indicated in the equation below [46,55],

$$\varepsilon = \varepsilon' + i\varepsilon' \tag{9}$$

The real part (ε′) depicts the dispersion of light within the material and the imaginary part (ε″) shows the energy absorbed by the movement of the dipole moment, and the following equations can be used to compute it using the n and k values [56,57],

$$\varepsilon' = n^2 - k^2 \tag{10}$$

$$\varepsilon'' = 2nk \tag{11}$$

The dependences of both factors, ε′ and ε″, on the incident photon energy are illustrated in Fig. 8. obviously ε′ and ε″ increases with increasing the UiO-66 additives to the Zn-BiOBr composite. The similarity between the behavior of the ε′ with refractive index and ε″ with *k* is evident. Moreover, ε′ value is larger than that for ε″. Increasing the UiO-66 additives to the Zn-BiOBr causes a change in polarization, resulting in high ε′ and low ε″ values and less energy dissipation.

A material's optical conductivity (σ_{opt}) indicates how the induced current density affects the electric field produced at random frequencies. [58]. The mobility of photo-generated carriers as an effect of the electromagnetic excitation, triggering optical conductivity and this parameter can be calculated using the following equation [58].

$$\sigma_{opt} = \frac{n\alpha c}{4\pi} \tag{12}$$

where (c=3×10^8 m/sec) is the light speed in free space. Fig. 9 depicts the correlation between the energy of incoming photons and $\sigma_{opt.}$. It can be observed that as the UiO-66 additives to the Zn-BiOBr increases the $\sigma_{opt.}$ increases. This might be due to the increase in α and *n* values of the material with increasing the UiO-66 additives to the Zn-BiOBr. At high photon energies, optical conductivity is enhanced due to the excitation of electrons by incident photons. The $\sigma_{opt.}$ value of MOF and Zn-BiOBr composite at 400 nm is about 3.42×10^9 and 8.37×10^9 sec^{-1}, respectively which increases to about 1.32 ×10^{10}, 1.66×10^{10}, and 2.48×10^{10} sec^{-1} for Zn-BiOBr with different UiO-66 contents (ZBU-10 %), (ZBU-20 %), and (ZBU-30 %), respectively.

The energy dispersion parameters play an important role in identifying the characteristics of optical materials. They can be used to calculate factors necessary for designing optical communication and spectral dispersion devices. Therefore, studying the energy of the effective single oscillator (E_o) and the dispersion energy (E_d) for the present system is imperative, which can be done using the Wemple-DiDomenico model as follows [53],

$$\frac{1}{n^2-1} = \frac{E_o}{E_d} - \frac{h\upsilon^2}{E_o E_d} \tag{13}$$

Plotting a graph between the refractive index factor 1/(n^2-1) on the y-axis and (hυ)^2 on the x-axis, as seen in Fig. 10 allows for the determination of E_o and E_d parameters, which are summarized in Table 2 based on the intercept and slope values. The E_o and E_d values increased by increasing the MOF content in the ZB systems.

Obviously, the E_o and E_d values increased as the UiO-66 content increases in the matrix. With these values it can be possible to calculate various nonlinear optical parameters as follows: [54,59];

$$f = E_d E_0 \tag{14}$$

$$athw = 0 \quad \rightarrow \quad n_0 = \sqrt{1 + \frac{E_d}{E_0}} \tag{15}$$

$$\varepsilon_s = n_0^2 \tag{16}$$

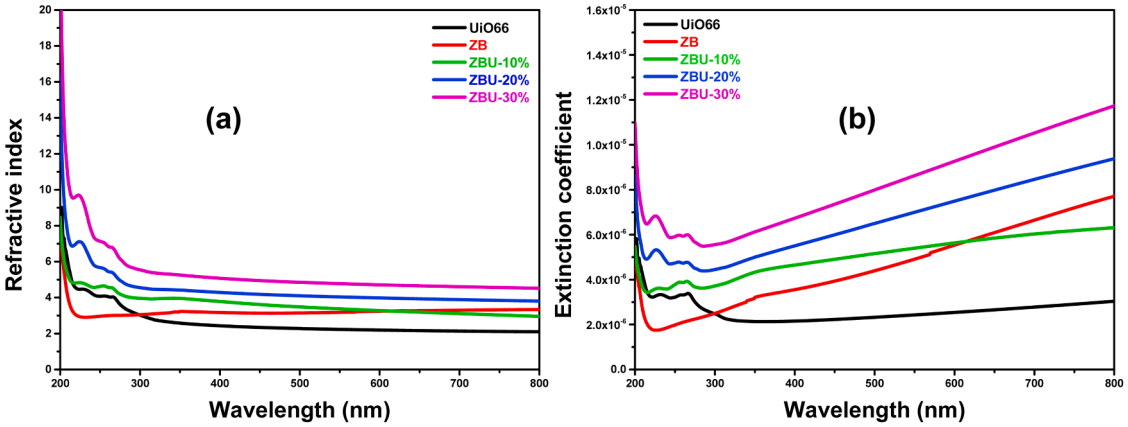

Fig. 7. Plots of (a) Refractive index and (b) extinction coefficient as a function of wavelength for Zn-BiOBr, UiO-66, ZBU-10 %, ZBU-20 %, and ZBU-30 %.

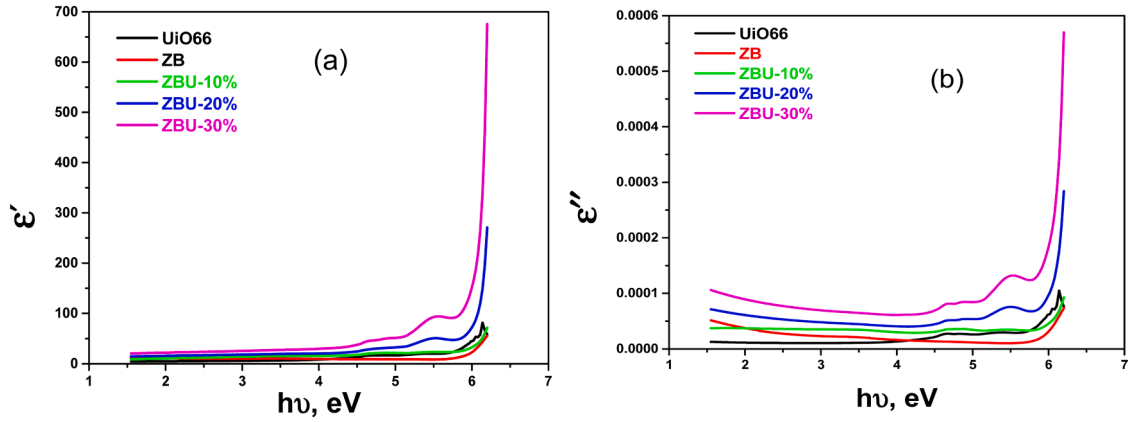

Fig. 8. Plots of (a) ε′ and (b) ε″ vs. hυ for Zn-BiOBr, UiO-66, ZBU-10 %, ZBU-20 %, and ZBU-30 %.

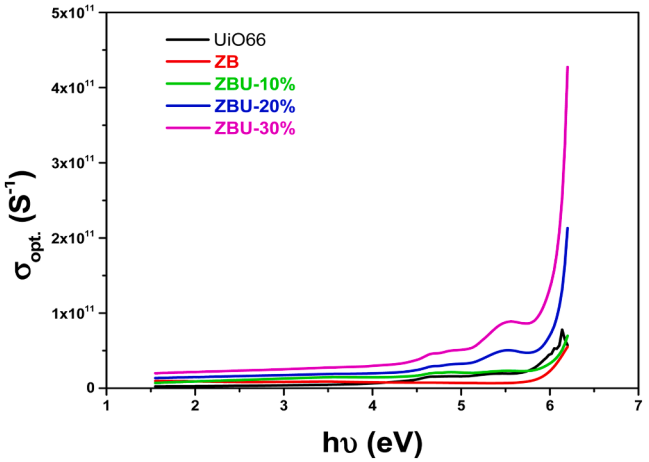

Fig. 9. The variation of $\sigma_{opt.}$ with (h υ) for Zn-BiOBr, UiO-66, ZBU-10 %, ZBU-20 %, and ZBU-30 %.

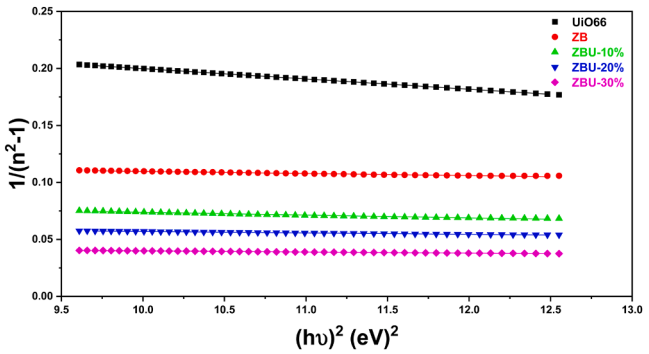

Fig. 10. $1/(n^2-1)$ vs. $(h\upsilon)^2$ for Zn-BiOBr, UiO-66, ZBU-10 %, ZBU-20 %, and ZBU-30 %.

$$\chi^{(1)} = \frac{E_d}{4\pi E_o} \tag{17}$$

$$\chi^{(3)} = 6.82 \times 10^{-15} \left[\frac{E_d}{E_o}\right]^4 \tag{18}$$

$$n_2 = \frac{12\pi\chi^{(3)}}{n_o} \tag{19}$$

where *f*, n_0, ε_s, first-$\chi^{(1)}$, third-$\chi^{(3)}$ order, and n_2 are the optical-oscillator strengths, static-refractive index, static-dielectric constant, nonlinear optical susceptibilities, and nonlinear refractive index, respectively. As shown in Table 2, all *f*, n_0, ε_s, $\chi^{(1)}$, $\chi^{(3)}$ order, and n_2 values enhanced with increasing UiO-66 content in the heterostructure. The $\chi^{(3)}$ value for ZB matrix is 2.52×10^{-11} increases to 1.11×10^{-9} after inclusion 30 % UiO-66 to the composite matrix, which is better outcome compared to TiO_2/ZnO thin film [54] and Se-Te-Bi thin film [55]. The n_2 increases with increasing linear refractive index (n) and decreasing (E_g) is related to an increase in metallicity (M). Besides, the high nonlinear refractive index possesses a metallization criterion of approximately 0.30–0.45 [58], compatible with the calculated values shown in Table 1. High values of $\chi^{(3)}$ and n2 for the present composite materials possess large applications in nonlinear optical devices.

4. Conclusion

Solvothermal process was used to prepare Zn-BiOBr and UiO-66 after that, the heterostructures between both materials were fabricated via simple wet chemical method. The phyico-chemical characterizations were confirmed the formation of heterostructure interface. Subsequently, the optical features were investigated and showing that, optical band gab of UiO-66, the refractive index, metallization values, and the optical electronegativity ($\Delta\chi$) were decreased upon conjugation with Zn-BiOBr while, The n and Λ values increased. Furthermore, As UiO-66 content increase in heterostructure, all *f*, n_0, ε_s, $\chi^{(1)}$, $\chi^{(3)}$ order, and n_2 values enhanced, enabling using these materials in a variety of nonlinear optical device applications.

Table 2
The calculated nonlinear optical parameters according to WDD model.

Sample ID	E_d	E_0	n_0	$es=n_0^2$	$f=E_0E_d$	$\chi^{(1)}$	$\chi^{(3)}$	n_2
UiO−66	19.54	5.67	2.109	4.45	110.74	0.27	9.63×10^{-13}	1.72×10^{-11}
ZBU−10 %	64.42	6.34	3.342	11.17	408.16	0.81	7.29×10^{-11}	8.22×10^{-10}
ZBU−20 %	107.33	7.45	3.924	15.40	800.00	1.15	2.93×10^{-10}	2.81×10^{-9}
ZBU−30 %	142.38	7.09	4.590	21.07	1010.10	1.60	1.11×10^{-9}	9.08×10^{-9}
ZB	64.73	8.31	2.965	8.79	537.63	0.62	2.52×10^{-11}	3.20×10^{-10}

CRediT authorship contribution statement

Mohamed Taha: Writing – review & editing, Supervision, Methodology, Investigation, Formal analysis, Conceptualization. **Nour Marwan M.:** Methodology, Investigation, Conceptualization. **A. Khalid:** Writing – review & editing, Methodology, Investigation, Formal analysis, Conceptualization. **T.S. Soliman:** Writing – review & editing, Investigation, Formal analysis, Conceptualization. **Hassan Nageh:** Supervision, Methodology, Investigation, Formal analysis, Conceptualization. **A. Farid:** Writing – original draft, Methodology, Investigation, Formal analysis, Conceptualization.

Declaration of Competing Interest

The authors declare that they have no known competing financial interests or personal relationships that could have appeared to influence the work reported in this paper

Data Availability

No data was used for the research described in the article.

References

[1] H. Furukawa, et al., The chemistry and applications of metal-organic frameworks, Science 341 (6149) (2013) 1230444.
[2] W.P. Lustig, S.J. Teat, J. Li, Improving LMOF luminescence quantum yield through guest-mediated rigidification, J. Mater. Chem. C. 7 (46) (2019) 14739–14744.
[3] R. Xiang, et al., A new type Co (II)-based photocatalyst for the nitrofurantoin antibiotic degradation, J. Mol. Struct. 1312 (2024) 138501.
[4] Y. Wu, et al., Synergistic efficacy unleashed: Co/Ni-based catalysts as a versatile powerhouse for photocatalytic degradation of ornidazole, Inorg. Chim. Acta 568 (2024) 122115.
[5] M.M. Khan, A. Rahman, S.N. Matussin, Recent progress of metal-organic frameworks and metal-organic frameworks-based heterostructures as photocatalysts, Nanomaterials 12 (16) (2022) 2820.
6 J.H. Cavka, et al., A new zirconium inorganic building brick forming metal organic frameworks with exceptional stability, J. Am. Chem. Soc. 130 (42) (2008) 13850–13851.
[7] C. Rao, et al., The extra-large calixarene-based MOFs-derived hierarchical composites for photocatalysis of dye: facile syntheses and contribution of carbon species, J. Alloy. Compd. 897 (2022) 163178.
[8] J.-C. Jin, et al., A 3D rare cubane-like tetramer Cu (II)-based MOF with 4-fold dia topology as an efficient photocatalyst for dye degradation, Colloids Surf. A: Physicochem. Eng. Asp. 656 (2023) 130475.
[9] O.K. Farha, et al., Metal–organic framework materials with ultrahigh surface areas: is the sky the limit? J. Am. Chem. Soc. 134 (36) (2012) 15016–15021.
[10] H. Deng, et al., Large-pore apertures in a series of metal-organic frameworks, science 336 (6084) (2012) 1018–1023.
[11] J. Lyu, et al., Metal–organic framework UiO-66 as an efficient adsorbent for boron removal from aqueous solution, Ind. Eng. Chem. Res. 56 (9) (2017) 2565–2572.
[12] A. Mohammadi, et al., Metal-organic framework Uio-66 for adsorption of methylene blue dye from aqueous solutions, Int. J. Environ. Sci. Technol. 14 (2017) 1959–1968.
[13] Y. Wang, et al., UiO-66-based metal organic frameworks for the photodegradation of acetaminophen under simulated solar irradiation, J. Environ. Chem. Eng. 9 (5) (2021) 106087.
[14] M. Bahmani, et al., UiO-66 (Ti)-Fe3O4-WO3 photocatalyst for efficient ammonia degradation from wastewater into continuous flow-loop thin film slurry flat-plate photoreactor, J. Hazard. Mater. 393 (2020) 122360.
[15] B. Ni, et al., Understanding the linear and second-order nonlinear optical properties of UiO-66-derived metal–organic frameworks: A comprehensive DFT study, J. Phys. Chem. C. 124 (21) (2020) 11595–11608.
[16] C.-Y. Chang, et al., Enhanced performance and stability of low-bandgap mixed lead–tin halide perovskite photovoltaic solar cells and photodetectors via defect passivation with UiO-66-NH 2, *Met. –Org. Framew. Interfacial Eng.* Mol. Syst. Des. Eng. 7 (9) (2022) 1073–1084.
[17] J. Li, et al., Solar water splitting and nitrogen fixation with layered bismuth oxyhalides, Acc. Chem. Res. 50 (1) (2017) 112–121.
[18] S. Singh, R. Sharma, M. Khanuja, A review and recent developments on strategies to improve the photocatalytic elimination of organic dye pollutants by BiOX (X= Cl, Br, I, F) nanostructures, Korean J. Chem. Eng. 35 (2018) 1955–1968.
[19] C. Gong, et al., Large-scale ultrathin 2D wide-bandgap BiOBr nanoflakes for gate-controlled deep-ultraviolet phototransistors, Adv. Mater. 32 (12) (2020) 1908242.
[20] M. Cai, A. Shui, B. Du, Constructing the ZnO/BiOBr hierarchical heterojunction for efficient pollutant photodegradation driven by visible-light, Surf. Interfaces 37 (2023) 102643.
[21] D. Li, et al., Improvement of photocatalytic activity of BiOBr and BiOBr/ZnO under visible-light irradiation by short-time low temperature plasma treatment, J. Alloy. Compd. 924 (2022) 166608.
[22] X. Meng, et al., Enhanced photocatalytic activity of BiOBr/ZnO heterojunction semiconductors prepared by facile hydrothermal method, Int. J. Photo 2015 (1) (2015) 747024.
[23] H.R. Ali, E.A. Motawea, Ternary photodegradable nanocomposite (BiOBr/ZnO/WO3) for the degradation of phenol pollutants: optimization and experimental design, ACS Omega 6 (34) (2021) 22047–22064.
[24] X.C. Song, et al., The solvothermal synthesis and enhanced photocatalytic activity of Zn 2+ doped BiOBr hierarchical nanostructures, N. J. Chem. 40 (1) (2016) 130–135.
[25] K. Ahmad, et al., Engineering of Zirconium based metal-organic frameworks (Zr-MOFs) as efficient adsorbents, Mater. Sci. Eng.: B 262 (2020) 114766.
[26] H. Tian, et al., BiOBr@ UiO-66 photocatalysts with abundant activated sites for the enhanced photodegradation of rhodamine b under visible light irradiation, Mater. Sci. Eng.: B 271 (2021) 115297.
[27] H. Tian, et al., BiOBr@ UiO-66 photocatalysts with abundant activated sites for the enhanced photodegradation of rhodamine b under visible light irradiation 271 (2021) 115297.
[28] J. Ding, et al., UiO-66 (Zr) coupled with Bi2MoO6 as photocatalyst for visible-light promoted dye degradation 497 (2017) 126–133.
[29] W. Li, et al., Constructing highly catalytic oxidation over BiOBr-based hierarchical microspheres: importance of redox potential of doped cations, Mol. Catal. 438 (2017) 19–29.
[30] G. Tang, et al., Constructing novel visible-light-driven ternary photocatalyst of AgBr nanoparticles decorated 2D/2D heterojunction of g-C3N4/BiOBr nanosheets with remarkably enhanced photocatalytic activity for water-treatment 45 (15) (2019) 19197–19205.
[31] X. Li, et al., Zr-MOFs based BiOBr/UiO-66 nanoplates with enhanced photocatalytic activity for tetracycline degradation under visible light irradiation 10 (12) (2020).
[32] F. Yu, et al., Visible-Light-Driven Zr-MOF/BiOBr Heterojunction for the Efficient Synchronous Removal of Hexavalent Chromium and Rhodamine B from Wastewater, ACS Omega 7 (29) (2022) 25066–25077.
[33] R.S. Salama, et al., Silver nanoparticles supported on UiO-66 (Zr): as an efficient and recyclable heterogeneous catalyst and efficient adsorbent for removal of Indigo Carmine 626 (2021) 127089.
[34] S. Chavan, et al., H 2 storage in isostructural UiO-67 and UiO-66 MOFs 14 (5) (2012) 1614–1626.
35 F. Ahmadijokani, et al., Superior chemical stability of UiO-66 metal-organic frameworks (MOFs) for selective dye adsorption, Chem. Eng. J. 399 (2020) 125346.
[36] Guo, J., *Design of hierarchically structured BiOBr-based photocatalysts and photoelectrodes for enhanced solar energy conversion*. 2019, University of Southampton.
[37] D. Van Le, et al., Synthesis of a UiO-66/gC 3 N 4 composite using terephthalic acid obtained from waste plastic for the photocatalytic degradation of the chemical warfare agent simulant, methyl paraoxon, RSC Adv. 12 (35) (2022) 22367–22376.
[38] Q. Hu, et al., Construction of NH2-UiO-66/BiOBr composites with boosted photocatalytic activity for the removal of contaminants, Colloids Surf. A: Physicochem. Eng. Asp. 579 (2019) 123625.
[39] S.-R. Zhu, et al., In situ growth of metal–organic framework on BiOBr 2D material with excellent photocatalytic activity for dye degradation, Cryst. Growth Des. 17 (5) (2017) 2309–2313.
40 M. Taha, et al., Nano Ag/AgBr/gC 3 N 4 catalyzed the production of hydrogen and reduction of d-glucose to sorbitol under visible light irradiation, N. J. Chem. 46 (37) (2022) 17746–17754.
[41] M. Taha, et al., Fabricating a 3D floating porous PDMS− Ag/AgBr decorated g-C3N4 nanocomposite sponge as a re-usable visible light photocatalyst, Sci. Rep. 14 (1) (2024) 4184.
[42] J. Guo, et al., Experimental and DFT insights of the Zn-doping effects on the visible-light photocatalytic water splitting and dye decomposition over Zn-doped BiOBr photocatalysts, Appl. Catal. B: Environ. 243 (2019) 502–512.
[43] M. Fiaz, et al., Synthesis of efficient TMS@ MOF-5 catalysts for oxygen evolution reaction, Catal. Lett. 150 (2020) 2648–2659.
[44] P.H. Andrade, et al., Band gap analysis in MOF materials: Distinguishing direct and indirect transitions using UV–vis spectroscopy, Appl. Mater. Today 37 (2024) 102094.
[45] Z. Yang, et al., Flower-like BiOBr/UiO-66-NH2 nanosphere with improved photocatalytic property for norfloxacin removal, Chemosphere 220 (2019) 98–106.
[46] Z.K. Heiba, et al., Investigation of the structural and linear/nonlinear optical characteristics of ZnO nanostructures alloyed with Co3O4 and NiO, J. Sol. -Gel Sci. Technol. 108 (1) (2023) 175–186.
[47] Y. Yang, et al., Construction of iodine vacancy-rich BiOI/Ag@ AgI Z-scheme heterojunction photocatalysts for visible-light-driven tetracycline degradation: transformation pathways and mechanism insight, Chem. Eng. J. 349 (2018) 808–821.
48] M. Halimah, et al., Optical basicity and electronic polarizability of zinc borotellurite glass doped La3+ ions, Results Phys. 7 (2017) 581–589.
[49] Chongad, L., et al., *Optical properties of CuS nanoparticles embedded polyvinyl alcohol (PVA) films*. 2021.
[50] R. Reddy, et al., Optical electronegativity and refractive index of materials, Opt. Mater. 10 (2) (1998) 95–100.
[51] A.M. Salem, et al., Effect of polypyrrole on structural, optical and thermal properties of CMC-based blends for optoelectronic applications, Opt. Mater. 134 (2022) 113128.

[52] M. Taha, et al., Controlling the shell thickness of SiO2 on TiO2 NPs: Characterization, linear and nonlinear optical properties, Ceram. Int. 50 (9) (2024) 15397–15406.
[53] A.S. Hassanien, A.A. Akl, Influence of composition on optical and dispersion parameters of thermally evaporated non-crystalline Cd50S50− xSex thin films, J. Alloy. Compd. 648 (2015) 280–290.
[54] S. Fouad, et al., ALD of TiO2/ZnO mutilayers towards the understanding of optical properties and polarizability, Opt. Laser Technol. 140 (2021) 107035.
[55] P. Yadav, A. Sharma, Investigation of optical nonlinearities in Bi-doped Se-Te chalcogenide thin films, J. Electron. Mater. 44 (2015) 916–921.
[56] T. Soliman, et al., Nanocomposite film combines polyvinyl alcohol and iron oxide capped in silica for optical applications, Opt. Quantum Electron. 56 (5) (2024) 786.
[57] T. Soliman, M. Taha, A. Khalid, Studying the Structural, thermal, mechanical, and dielectric features of PVA/iron oxide@ SiO2 polymer nanocomposites for electrical applications, Mater. Chem. Phys. (2024) 129644.
[58] V. Dimitrov, S. Sakka, Linear and nonlinear optical properties of simple oxides. II, J. Appl. Phys. 79 (3) (1996) 1741–1745.
[59] A. Khalid, et al., Fe3O4 nanoparticles and Fe3O4@ SiO2 core-shell: synthesize, structural, morphological, linear, and nonlinear optical properties, J. Alloy. Compd. 947 (2023) 169639.